Microstructure and defect sensitivities in the very high-cycle fatigue response of Laser Powder Bed Fused Ti–6Al–4V

Grégoire Brot, Imade Koutiri, Vincent Bonnand, Véronique Favier, Corinne Dupuy, Nicolas Ranc, Patrick Aimedieu, Fabien Lefebvre, Robin Hauteville

Microstructure and defect sensitivities of LPBF manufactured Ti-6Al-4V in accelerated 20 kHz fatigue response

Grégoire Brot[a,b,1,*], Imade Koutiri[b], Vincent Bonnand[a], Véronique Favier[b], Corinne Dupuy[b], Nicolas Ranc[b], Patrick Aimedieu[c], Fabien Lefebvre[d], Robin Hauteville[d]

[a] *DMAS, ONERA, Université Paris Saclay, 29 Avenue de la Division Leclerc, Châtillon, France*
[b] *PIMM, Arts et Metiers Institute of Technology, CNRS, Cnam, HESAM University, 151 Boulevard de l'Hopital, Paris, France*
[c] *Université Paris-Est, Laboratoire Navier, CNRS UMR8205, ENPC, IFSTTAR, 6 et 8 avenue Blaise Pascal, 77455 Marne-la-Vallée Cedex, France*
[d] *CETIM, 52 Av. Félix Louat, Senlis, France*

Abstract

Additive manufacturing processes such as the Laser Powder-Bed Fusion (LPBF) are associated with a large number of process parameters. Many of them can influence the microstructure or the porosity of the produced parts and consequently their high and very high cycle fatigue (VHCF) properties. In this context, process parameter optimization in regards to VHCF resistance requires accelerated fatigue testing methods such as ultrasonic fatigue testing. However, the defect and microstructure sensitivities of additively manufactured materials in accelerated 20 kHz fatigue response needs to be studied. This works aims to analyze this sensitivity and the effects of microstructure and porosity on the VHCF behavior of LPBF-Ti-6Al-4V. To do so ultrasonic fatigue testing is performed on five grades of LPBF-Ti-6Al-4V that have different porosity levels or microstructures. These grades were generated using different LPBF process parameters and different thermal post-treatments. It was found that both material features highly influenced the VHCF properties of LPBF-Ti-6Al-4V revealing the sensitivity of accelerated 20 kHz fatigue tests to these features. Furthermore, both the size of porosity and the size of grains have a first order effect on fatigue strength. These sizes control the type of fatigue crack initiation. Moreover, an optimal temperature of thermal treatment for VHCF properties of LPBF-Ti-6Al-4V was found to be close to 920°C.

Keywords: Very high cycle fatigue, Titanium alloy, Microstructures, Porosity, Tomography

1. Introduction

Ti-6Al-4V is the most used titanium alloy with a wide range of applications thanks, among others, to its high strength to weight ratio or fatigue strength. Additive manufacturing (AM) of this alloy using Laser Powder Bed Fusion (LPBF) is a relatively mature technology. Ti-6Al-4V is indeed one of the most studied alloy in additive manufacturing

*Corresponding author: gregoire.brot@ensam.eu, +33 689618195
Email addresses: gregoire.brot@ensam.eu (Grégoire Brot), imade.koutiri@ensam.eu (Imade Koutiri), vincent.bonnand@onera.fr (Vincent Bonnand), veronique.favier@ensam.eu (Véronique Favier), corinne.dupuy@ensam.eu (Corinne Dupuy), nicolas.ranc@ensam.eu (Nicolas Ranc), patrick.aimedieu@enpc.fr (Patrick Aimedieu), fabien.lefebvre@cetim.fr (Fabien Lefebvre), robin.hauteville@cetim.fr (Robin Hauteville)

with more than 1800 research articles on ScienceDirect website mentioning "Ti-6Al-4V" and "LPBF" (or "SLM"). Printed pieces have now porosity usually lower than 0.5 % [1][2]. Nevertheless, significant dispersion of pore size are observed within and in between LPBF printing batches [3] and pore size strongly affects high and very high cycle fatigue (HCF, VHCF) strength [3][4][5]. Furthermore, Spears and Gold [6] identified 50 key process parameters in LPBF and many of them can affect the fatigue strength through porosity or microstructural changes. In this context, parameter optimization in regards to fatigue strength is a huge challenge because of long testing time. This duration can be significantly reduced using ultrasonic fatigue machines that allow fatigue testing at 20 kHz. However, the sensitivity of VHCF properties in accelerated 20 kHz fatigue response to the specific microstructure and porosity of AM materials was not studied yet. Therefore, in this work ultrasonic fatigue is used to study the VHCF properties of LPBF parts. Some of the tested parts were printed using manufacturing parameters that generate a minimal porosity and some were printed using parameters that lead to degraded porosity. In addition to their different porosity levels, tested parts had distinct microstructures generated by different post heat-treatments.

During LPBF process the small meltpool size and the relatively high scanning speed of the laser lead to very high cooling rates from 10^3 to $10^8 K/s$ [7]. As the result, the microstructure of as-built Ti-6Al-4V is an ultrafine lamellar one. Ti-6Al-4V is an $\alpha + \beta$ titanium alloy at room temperature. Above β-transus temperature $T_\beta \approx 1000°C$, it is fully composed of β phase. According to X-ray diffraction (XRD) analysis from [2][8][9], the as-built microstructure is only composed of martensitic α' phase. During printing process, each point of LPBF part is subjected to successive heating and cooling phases as layers are deposited and laser-scanned. Yang et al. [10] studied this specific thermal history and its effects on the formation of α' phase. As-built microstructure present a hierarchical structure composed of four types of martensite α'-lamellae with a decreasing size. Primary lamellae are the largest ones with a width from 1 to 3 µm. Moreover, two main types of porosity can be found in LPBF parts: lack of fusion pore and spherical gas pore. The different mechanisms causing the formation of these pores are detailed in [11]. The first ones have an irregular shape, are often filled with unmelted powder particle and tend to be larger in the plane perpendicular to building direction. They can be formed when the laser bring insufficient energy to the powder. The second ones have a regular and spherical shape. Spherical gas pore can be subdivided between blowhole pore and keyhole pore. Blowhole pores are gas bubble trapped during solidification with a maximal size of 30 to 50 µm. Keyhole pores are large and spherical ones that are formed during the collapse of the vapor capillary that appear when the welding mode is a keyhole mode [11]. This welding mode appears with high laser intensity.

Furthermore, as-built LPBF parts retain high residual stresses also related to the high cooling rate and the layer by layer heating process. Leuders et al. [12] found out using XRD that these stresses are tensile ones at the surface with a magnitude from several hundred MPa in the as-built state. These are negligible when parts are treated at 800°C for 2h. Similar results were obtained by Syed et al. [13] using the contour method. They found out a 90 % reduction of stresses when treated at 680°C for 3h. It is therefore relevant to study the thermal post-treatment for this material. Annealing treatments at sub β-transus temperature have two main effects on LPBF-Ti-6AL-4V microstructure. The first one is the decomposition of the metastable phase α' into $\alpha + \beta$ phases. Kaschel et al. [14] showed using in-situ

high temperature XRD that the decomposition appeared above 500°C and is fully completed when treated at 750°C. According to Etesami et al. [15] α' martensite is fully decomposed after 2h at 900°C. When treated at 900°C, β phase is formed as both particles and rod-shaped. When treated at 611°C β phase precipitated mostly into fine particles. The second main effect of sub β-transus annealing treatment is the coarsening of α/α' lamellae. In these microstructures each α/α' lamellae correspond to a crystallographic grain. Vrancken et al. [9] showed that temperature has a greater impact on lamellae coarsening than resident time or cooling rate for treatment below β-transus. Width of lamellae goes from 1.22 to 2.23 µm for treatment at 850 to 940°C. In the case of super transus-β treatment, primary β grains become equiaxed as reported in [9][16]. For sufficiently low cooling rate, colonies of $\alpha+\beta$ lamellae are formed out of high temperature β grains. Ter Haar et al. [17] showed using electron backscatter diffraction (EBSD) that each colony of $\alpha+\beta$ lamellae is a grain as it has a unique crystallographic orientation.

The specific microstructure of LPBF-Ti-6Al-4V affects its mechanical properties. Several authors [9][12][15][18] studied the effect of heat-treatment on its mechanical properties. As-built LPBF-Ti-6Al-4V shows an higher tensile strength but a lower fracture elongation compared to conventionally manufactured one [2]. With an increasing temperature of treatment, yield strength tends to decrease while fracture elongation increases. According to Etesami et al. [15], ductility increase and yield strength decrease are related to the martensite decomposition during which volume fraction of the more ductile β phase increases while the one of brittle α' phase decreases. Zhang et al. estimated a β volume fraction of 3 % (resp. 8 %) after treatment at 730°C (resp. 900°C). For treatment temperatures higher than 800°C, once α'martensite is fully decomposed, ductility increase is related to the growth of α laths [15].

Concerning fatigue, Bathias and Paris [19] showed that some parts in the aeronautical industry, the main application domain of Ti-6Al-4V, are loaded in high and very-high cycle fatigue. It is therefore of a great interest to study the HCF and VHCF behavior of this alloy. According to the review from Li et al. [20], process-induced porosity and surface quality appear to have the greatest effect on fatigue strength of LPBF-Ti-6Al-4V. Kasperovich and Hausmann [1] found a significant fatigue life increase between as-built and machined specimens but a similar fatigue life between machined specimens and specimens that were both heat-treated and machined. However, thermal treatments also impact fatigue strength [20]. For comparison purpose, we plotted in Figure 1 the effect of thermal post-treatment on the HCF performance of machined or polished LPBF-Ti-6Al-4V based on testing results collected in [1][21][22][23][24][25][26][27][28]. The results for forged Ti-6Al-4V with a duplex microstructure were also plotted. These results show a high scatter within each study and in between different studies. For example, scatter, evaluated as the standard deviation associated with a log-normal distribution of stresses at 10^7 cycles, is 30 MPa (resp. 50 MPa) for the "Stress-relieving" (resp. "Sub-transus annealing") series of data in Figure 1. Le et al. [3] explained this scatter because of the different sizes and types of pores acting as fatigue crack initiation sites. Scatter is reduced when using hot isostatic pressing (HIP) treatment as it allows to close most of the process-induced pores, leading to superior fatigue properties [1][21] (Figure 1). Several authors used the Kitagawa-Takahashi (KT) diagram, originally proposed in [4], in order to analyze the effect of the size of pores on the fatigue limit of LPBF-Ti-6Al-4V. Le et al. [3] and Hu et al. [29] proposed a generalized KT diagram including fatigue life beside applied stress and size of

defects. Using this, Le et al. showed that crack initiation on internal pores leads to a significantly higher fatigue life than initiation on surface pores with the same size and tested under the same stress amplitude. Furthermore, this generalized diagram did not discriminate sample printed in different building directions meaning that the anisotropy of fatigue strength is only related to the apparent size of pores relative to the loading direction. As both the type and location of pore influence fatigue life, Le et al. proposed a ranking of critical defect types. The most harmful ones are surface lack of fusion followed by internal lack of fusion, surface gas pore and internal gas pore. Furthermore, fatigue crack growth models are another possible tool to assess defect severity in AM materials. Macallister and Becker [30] proposed a damage tolerant model in application to LPBF-Ti-6Al-4V. Using their model, they showed that fatigue strength was shown to be most sensitive to fatigue crack growth threshold. Moreover, the proposed model account for defect size, proximity to the free surface or crack closure effects.

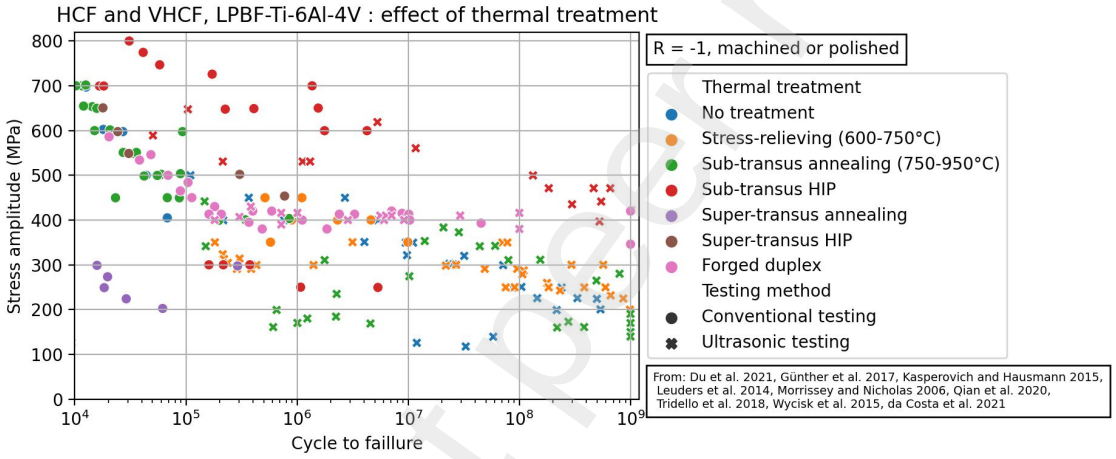

Figure 1: High and very high cycle fatigue results showing the effect of thermal treatment on the fatigue strength of LPBF-Ti-6Al-4V. Specimens are either machined or polished. For all, load ratio is $R = -1$. Results collected from [1][21][22][23][24][25][26][27].

The effect of sub-β-transus treatment on fatigue performance is complex. Indeed, grain coarsening and yield strength reduction should reduce fatigue strength while residual stress relieving and ductility increase tend to increase it. To the best of our knowledge, fatigue properties of stress relieved (treated at 600 to 750°C) parts and sub β-transus annealed (treated at 750 to 950°C) parts were never compared within the same study. Furthermore, super-β-transus treatment or super-β-transus HIP lead to reduced fatigue strength related to an excessive grain growth and reduced yield strength [21]. Results presented in Figure 1 highlight the fact that many process of post-process parameter can influence the fatigue strength of this material. Studying the effect of each parameter requires long testing campaign unless rapid testing method are used. LPBF-Ti-6Al-4V was studied in VHCF regime using ultrasonic fatigue. Wycisk et al. [26] and Günther et al. [23] performed both high and very-high cycle fatigue tests up to 10^9 cycles. Fatigue strength is still decreasing in the VHCF regime without showing any asymptotic behavior whereas results for forged material are clearly asymptotic for fatigue life higher than 10^6. In these studies [23][26], both conventional and ultrasonic fatigue tests were performed and no significant effect of the testing frequency was noticed by the authors.

In the VHCF regime, crack initiation of almost all specimens is internal whereas most of it were at the surface in the HCF regime. For HIPed specimens in [23], fatigue crack initiation is located on facets of α phase without any visible pore. More recently, Chi et al. [31] studied VHCF crack initiation using ultrasonic fatigue under two stress ratios ($R = -1$ or $R = 0.5$). For $R = -1$, fatigue life diagram is a multi-stage one as defined in [32]. Indeed, cracks initiated on surface in the HCF regime whereas they initiated in the bulk in the VHCF regime. In the case of internal crack initiation, only specimens tested with a load ratio of $R = -1$ presented near crack origin a nanograin layer, visible as a rough area on fractography.

The present works aims to study the defect and microstructure sensitivities of the accelerated 20 kHz fatigue response of AM materials. At the same time, this work aims to investigate the effect of microstructure and porosity on the VHCF behavior of LPBF-Ti-6Al-4V. To do so ultrasonic fatigue testing is performed on five grades of LPBF-Ti-6Al-4V that have different porosity levels or microstructures. This allows separately studying the effect of these two material features as both are known to affect fatigue properties. Prior to fatigue testing, the five materials grades were characterized using microtomography, EBSD, electron microscopy and monotonic tensile testing. Following fatigue testing, fractographic analysis were performed.

2. Methods

2.1. Sample processing and microscopic analysis

Specimen preparation aims to produce five grades of LPBF-Ti-6Al-4V that have different microstructures and porosity levels. Three grades should have the same porosity level but different microstructures and three grades should have different porosities but the same microstructure. The different processing routes used to get these grades are presented in Figure 2. First, two porosity levels, noted P_1 and P_2, are generated during LPBF process with different laser scan strategies. Then, the different microstructures are generated with different thermal treatments. The third porosity level, noted P_0, is obtained using an Hot Isostatic Pressing (HIP) treatment.

All specimens were vertically printed as round bars using a SLM125 machine (SLM Solutions GmbH). Powder used is a Ti-6Al-4V from 3D SYSTEMS (LaserForm® Ti Gr5 (A)). 10 % (resp. 90 %) of powder particle size is lower than 20 µm (resp. 57 µm). LPBF process was done using a laser power of 275 W, an hatch distance of 120 µm, a scan speed of 1100 mm/s and a layer thickness of 30 µm. Building plate temperature was 150°C. During printing process, the "Sky-Writing" mode was deactivated. This mode enables to move the scanner at full speed all along the vector length while without it, the scanner accelerates and decelerates at each vector extremity. Therefore, the laser brings more energy to the powder at those locations and the high energy intensity leads to likelier formation of keyhole pores. In order to get parts with a porosity $P_2 \approx 1$ % and a quasi-homogeneous distribution of pores in the bulk, a chessboard scanning strategy and an inter-layer rotation of 15° are used. Width of chessboard pattern is equal to 3 mm. Part with a porosity P_1 are processed with laser track going through the part width and have in their bulk a porosity close to 0.001 %. Many large pores are produced at the edges of parts but these are removed during

post-processing. Specimens were fabricated within five printing batches. Cylinders with a length of 100 mm and a diameter of 13 mm were printed for tensile testing. For ultrasonic fatigue testing, printed cylinders are 80 mm long with a 13 mm diameter.

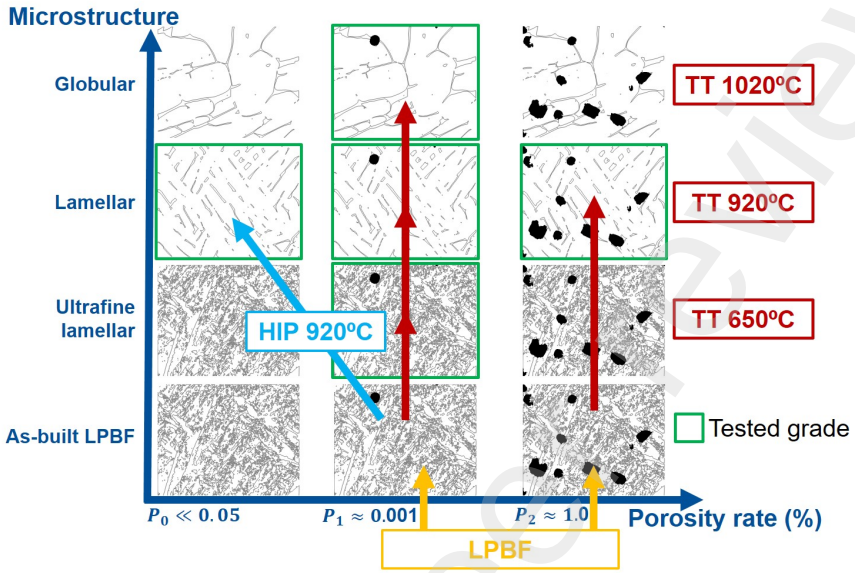

Figure 2: Different processing routes used to get specimen with different porosity levels or microstructures. HIP stands for hot isostatic pressing treatment. TT stands for thermal treatment.

All samples are then heat-treated (Figure 2). Parts with a porosity P_2 were treated at 920°C for 2h followed by furnace cooling. Parts printed with a porosity P_1 were divided into four groups randomly distributed within all printing batches. The first group was treated at 650°C for 3h followed by air cooling, the second one is treated at 920°C for 2h followed by furnace cooling, the third one is treated at 1020°C for 2h followed by furnace cooling and the forth group was HIPed at 920°C at a pressure of 2000 bar for 2h. During furnace cooling and HIP cooling, average cooling rate from high temperature to 500°C was close to 0.04°/s. The five material grades are noted in the following according to their porosity level and treatment temperature: P_0_920°C, P_1_650°C, P_1_920°C, P_1_1020°C and P_2_920°C. Specimens were then machining to their final geometry presented in Figure 3. Then, VHCF specimens were polished with paper grit up to 4000. Some cubic samples were also processed for microstructural analysis. Backscatter electron (BSE) microscopy and EBSD analysis were performed with a TESCAN MIRA microscope. EBSD view field was 700×700 µm with a spatial resolution of 500 nm.

Porosity of some specimens was analyzed using microtomography at the Navier laboratory in France. The micro-tomograph was an Ultratom made by RX Solutions, equipped with a L10801 X-ray source (max 230kV) and a Varex 4343 DX-I imager (3052 x 3052 active pixels, pixel size is 139 microns). Acceleration voltage was set to 140kV, current was 28 µA. Imager frame rate and averaging were respectively 1 and 8 and 2368 projections were acquired per sample. Samples were scanned with a voxel size of $4 \times 4 \times 4\,\mu m^3$. Successive sample scans were automatized by

placing samples in column in the tomograph and performing scans automatically one after another. Sample positioning was fixed to avoid motion during scan, by using long carbon fiber stems, which were attached to the column of samples from top to bottom.

As the size of pores and voxel were close, a simple binarization of tomographic data was not suited to estimate porosity and the size of pores. Therefore, two threshold grey levels were defined for each scanned sample: I_{metal} and I_{void}. These thresholds were defined using grey level profile across pores. When $I_{voxel_i} \geq I_{metal}$, $voxel_i$ was considered as only composed of metal. When $I_{voxel,i} \leq I_{void}$, $voxel_i$ was considered as only composed of void. For $I_{void} \leq I_{voxel_i} \leq I_{metal}$, $voxel_i$ was considered as partially composed of metal and void fraction was estimated to vary linearly between 1 for I_{void} and 0 for I_{metal}. The volume of each pore was obtained by summing each voxel volume times their void fraction. For each pore, equivalent size was calculated as $\sqrt[3]{Volume}$. Pore volume relative error was estimated as:

$$\frac{\sigma(Volume)}{Volume} = \frac{1}{\sqrt{N}} \frac{\sigma(I_{scan})}{I_{metal} - \bar{I}} \quad , \tag{1}$$

where $\sigma(I_{scan})$ is the standard deviation of grey levels in a fully dense region of the scan, N is the number of voxels describing the considered pore and $\bar{I}$ is the mean grey levels within the pore. Pore size error was estimated to correspond at maximum to 10 % when their volume was greater than 15 voxels ($\sqrt[3]{Volume} \approx 10\,\mu m$). Only pores larger than 15 voxels were considered during data processing. Ratio of porosity was estimated by considering only those pores. This was done to avoid counting noisy isolated voxels as void. Similarly to $\sqrt{Area_{eff}}$ method [5], data processing considered group of pores separated from a distance lower than the size of the smallest pore as one unique pore. Their size was defined from the smallest convex volume that surround all pores of the group. To study the distribution of large pores, block maxima strategy as defined in [29] was used. Scanned volume was divided into 60 sub-volumes. For each sub-volume, the size of the largest pore which centroid is in the sub-volume was collected.

2.2. Tensile and very high cycle fatigue testing

All mechanical tests were performed at room temperature. For each material grade, one specimen was used for tensile testing. Specimen geometry is presented in Figure 3.a. Tests were done on a servo-hydraulic machine. Tensile testing was a two imposed strain rates test followed by a relaxation step. This was done to evaluate the yield stress and the strain rate sensitivity of the different material grades. Strain rate was $10^{-2}\,s^{-1}$ until strain reached 2 % then strain rate was suddenly changed to $10^{-3}\,s^{-1}$ until strain reached 4 %, strain rate was then back to $10^{-2}\,s^{-1}$ until 5 %. This last strain was then maintain for 5 minutes for the relaxation test. Vickers microhardness test were also performed on each grade.

For each material grades, seven to ten fatigue specimens were tested with an ultrasonic fatigue machine. During testing, the machine imposes a sinusoidal displacement at 20 kHz to the specimen. This one vibrates in its first longitudinal eigenmode corresponding to a load ratio $R = -1$. Using modal finite element analysis, specimen were design so that this mode is close to the working frequency of the machine (Figure 3.b-c). Material behavior was

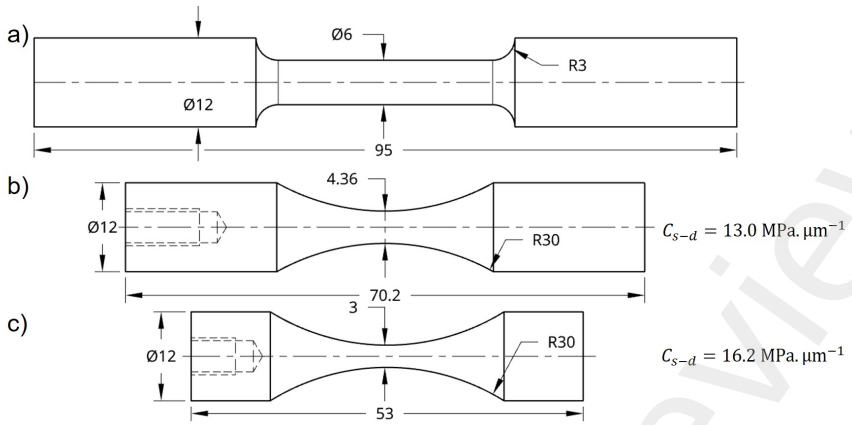

Figure 3: Geometry of specimen used for: a) tensile testing, b) for ultrasonic fatigue with a displacement-stress factor of 13 MPa/µm and c) for ultrasonic fatigue with a high factor of 16.2 MPa/µm (in mm).

supposed to be linear elastic meaning that the stress amplitude at the center of the specimen is linear with the imposed displacement amplitude. The stress-displacement factor was determined using an harmonic analysis at the working frequency by taking the mean stress amplitude over the central section for an imposed displacement amplitude (Figure 4). See [33] for more details on the designing step. As the fatigue strength of P_0_920°C specimens is higher than the ones of other grades, their design is the one in (Figure 3.c) so that the stress-displacement factor C_{s-d} is 16.2 MPa/µm. The design of all other specimens is the one in Figure 3.b associated with a factor C_{s-d} of 13 MPa/µm (Figure 4).

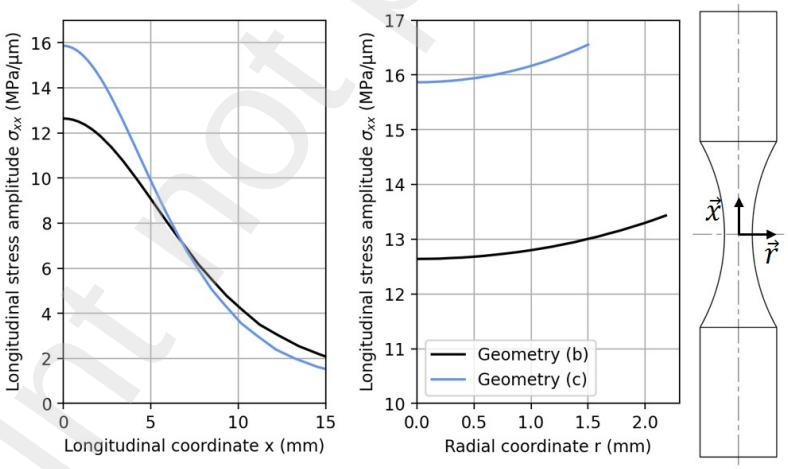

Figure 4: Longitudinal stress amplitude field within ultrasonic fatigue specimens calculated using an harmonic analysis finite element simulation. Imposed displacement is sinusoidal with an amplitude of 1 µm and a frequency of 20kHz. Geometry (b) and (c) are presented in Figure 3.

Tests were performed with a homemade machine, which is based on a piezo-electric converter 2000 Series Model CR-20 from Branson^{TM}, see [33] for further details on the testing setup. During fatigue test, displacement amplitude at the free end of specimen was measured using a HSV 2001 laser vibrometer. The stabilized temperature of the specimens did not exceed 40°C thanks to a forced convection cooling system. When a sufficiently large fatigue crack

appears in the specimen, the ultrasonic machine stops due to the induced frequency drop. Stress amplitude levels were chosen in order to get a stress to cycles to failure (SN) curve near $10^7 - 10^9$ cycles. To determine the corresponding stress level, the first specimen of each material grade was tested with a Locati procedure in which loading steps lasted 10^7 cycles and stress was increased by 10 MPa between two steps until specimen failed. For the other specimens used to get a SN curve, testing was done at a constant stress amplitude until failure. Test was stopped if it reaches 10^9 cycles. Specimens that failed were then cooled in liquid nitrogen and broken. During fractography analysis, the size of critical pore was determined using $\sqrt{Area_{eff}}$ method which is based on the projected area of the defect in the plan perpendicular to loading direction [5][34]. Defects were considered as internal ones if the distance between surface and crack initiation $d_{surface}$ was higher than the defect size $\sqrt{Area}$. They were considered as sub-surface ones if $\sqrt{Area} > d_{surface}$. For these ones, the effective area $\sqrt{Area_{eff}}$ which includes the defect and the ligament between defect and surface was considered.

3. Results

3.1. Microstructure and porosity analysis

Figure 5 presents BackScatter Electron (BSE) micrographs of the studied microstructures. Microstructure after the 650°C stress relieving treatment is visible in Figure 5.a. The as-built martensite phase α' is partially decomposed into $\alpha + \beta$ [35]. Indeed, BSE micrographs show fine and non-continuous β-phase around α/α' phase. Gil et al. [36] studied this decomposition during annealing treatment of forged Ti-6Al-4V. Most of α' should be decomposed for treatment at 650°C for 3h. The present microstructure is an ultrafine lamellar one, where the morphology of α/α'-lamellae remains close to the one of as-built α'-lamellae. The mean width of α/α'-lamellae evaluated on BSE micrographs is 0.4 µm. Proportion of β phase was estimated to 3 % using image processing of BSE micographs. Inverse pole figure of EBSD analysis can be seen in Figure 6.a. Groups of lamellae originated from the same prior β grain have a significant texture as discussed in [8]. However, direct pole figure of the 700×700 µm EBSD scan did not show any significant texture (Figure 6.d).

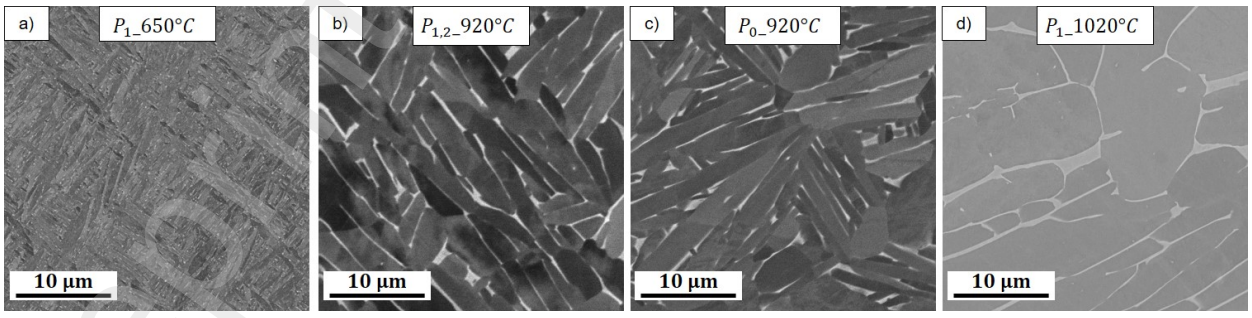

Figure 5: BackScatter Electron micrographs at the same scale of LPBF-Ti-6Al-4V microstructure when, a) treated at 650°C for 3h and air cooled, b) treated at 920°C for 2h and furnace cooled, c) HIPed at 920°C and 2000 bar for 2h, d) treated at 1020°C for 2h and furnace cooled. β-phase is the lighter phase.

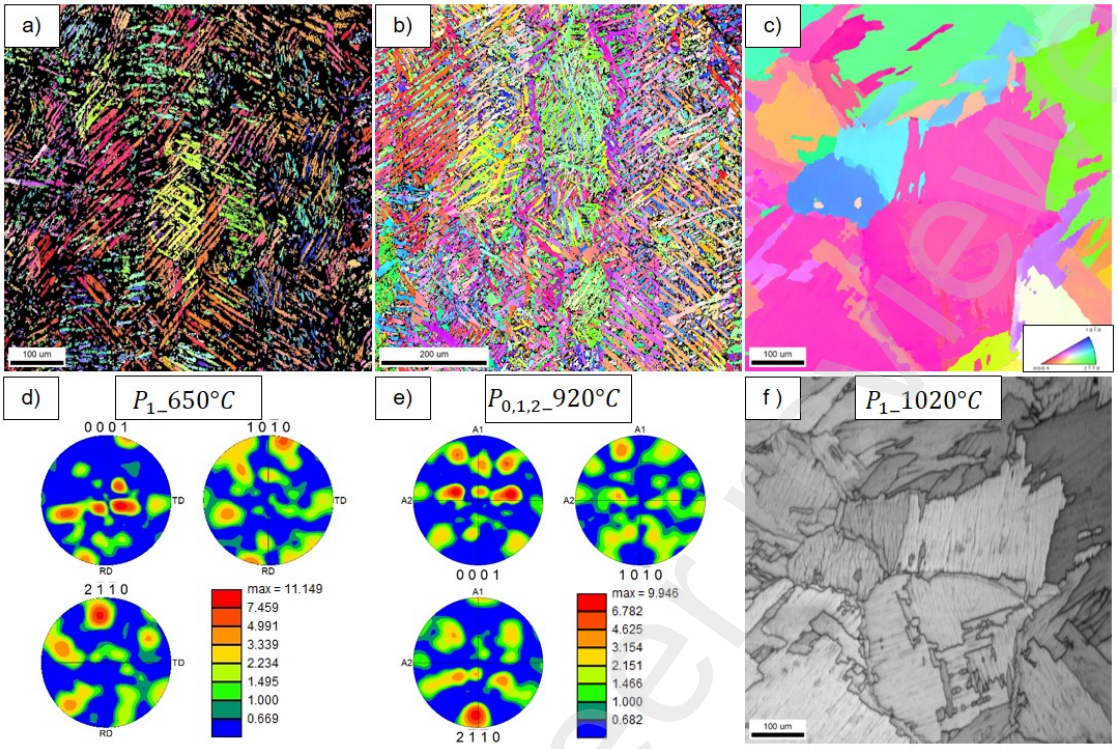

Figure 6: Inverse and direct pole figures from EBSD analysis on Titanium-α phase for samples treated: a) and d) at 650°C for 3h and air cooled, b) and e) at 920°C for 2h and furnace cooled, c) at 1020°C for 2h and furnace cooled. f) Image quality map of the scan c). Scale of inverse pole figures is the same. Building direction during LPBF process is vertical on inverse pole figures.

Microstructure after thermal treatment or HIP at 920°C is lamellar in which α-lamellae are 1.6 µm wide. According to [15][14] martensite α' should be fully decomposed into $\alpha + \beta$. The as-built hierarchical structure with primary to quaternary α'-lamellae can no longer be visible as the width of all α-lamellae is similar. β phase is present as thin bands that are 200 to 800 nm wide. Proportion of β phase was estimated to 8 % on BSE micrographs. Similarly to the first microstructure, groups of textured lamellae are visible in Figure 6.b without significant texture when analysing the whole scan (Figure 6.e). No significant difference between the microstructure obtained after the 920°C treatment or after the HIP treatment is visible. The microstructure after treatment at 1020°C is composed of colony of $\alpha + \beta$ lamellae that have the same orientation gathered in a grain (Figure 6.c). These grains are equiaxed and are 100 to 300 µm wide. Mean width of α (resp. β) lamellae is 5 µm (resp. 0.5 µm). β-phase is rod-shaped whereas it is present as rod-shaped and particles after sub β-transus treatment followed by air cooling [15]. Lamellae of the same colony can be visible on the image quality map of EBSD scan in Figure 6.f.

Table 1 presents the results of tomographic analysis. Size of pores was calculated as $\sqrt[3]{Volume}$ and only pores for which $\sqrt[3]{Volume} > 10\,\mu m$ were considered. In table 1, estimation of error on the ratio of porosity was based on the error on each pore volume (Equation 1). As no pore were detected in P_0 samples, error on porosity ratio could not be estimated. Pore size error is less than 1 µm for largest pore in each sample as many voxels describe these pores.

Block maxima strategy was used to get the distribution presented in Figure 7. This corresponds to the distribution of largest pores in sub-volumes represented using Gumbel reduced variate: $y_i = -\ln(-\ln(i/(n+1)))$ with n the number of sub-volumes and i the i-th local maximum from the smallest one. The quasi-linear aspect of these curves means that these distributions can be represented using Gumbel distribution. This distribution of the statistic of extreme allows to described the maximum values of a distribution. For more details on block maxima strategy see [29]. In Figure 7, data with a defect size of 0 µm correspond to sub-volumes in which no pores were detected. Although ratios of porosity of sample printed using P_1 parameter are different (Table 1), the size of their largest pore and their Gumbel distribution are similar. Meaning that this porosity level is reproducible and not affected by thermal post-treatment. Moreover, spatial distribution of pores was homogeneous in each scanned sample.

Table 1: Results of microtomographic analysis of porosity. Two specimens from each material grade excepted P_2_920°C were scanned.

Grade	P_0_920°C	P_1_1020°C	P_1_650°C	P_1_920°C	P_2_920°C
Ratio of porosity (ppm)	< 1	2 ± 0.2	3 ± 0.1	11 ± 0.4	10713 ± 20
Largest pore (µm)	< 10	36	51	44	260
Pore (>10 µm) density (mm^{-1})	0.0	0.7	0.6	2.2	117.3
Ratio of porosity (ppm)	< 1	2 ± 0.1	2 ± 0.1	3 ± 0.2	
Largest pore (µm)	< 10	35	24	33	
Pore (>10 µm) density (mm^{-1})	0.0	0.4	0.7	0.6	

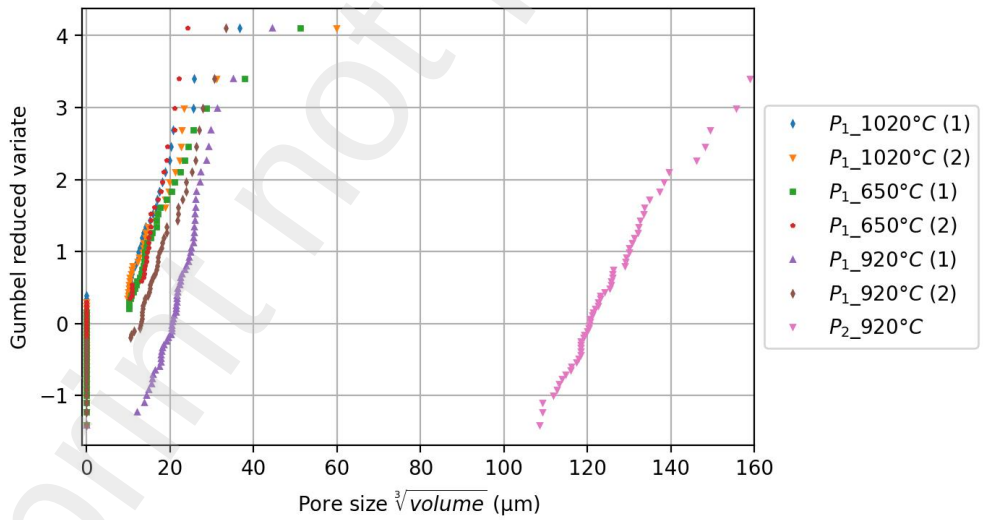

Figure 7: Distribution of largest pores in sub-volumes of tomographic scans.

3.2. Mechanical properties

Stress-strain curves of the tensile tests are represented in Figure 8. Table 2 presents for each grade the size of grain, the porosity, the yield stress at 0.2 % of plastic strain, the viscous stress relaxed during the 5 minutes relaxation at a strain of 5 % and the microhardness. The specimen of $P_1\_650°C$ grade broke outside the gauge of extensometer before relaxation step. Other specimen did not fail during test. The different microstructures strongly affect tensile behavior. Relationship between grain size d and yield stress σ_y follows Hall-Petch relationship: $\sigma_y = \sigma_0 + \frac{k}{\sqrt{d}}$ with $\sigma_0 = 830\,\text{MPa}$ and $k = 250\,\text{MPa}\sqrt{m}$. Compared to microstructure, porosity has a lower impact on tensile behavior. Yield stress is reduced by 5 % (55 MPa) when porosity goes from $P_0 \approx 0$ % to $P_2 \approx 1$ %. It can be noted that this reduction is not linear with the ratio of porosity. Close values of viscous stress and close stress drop at 2 % strain were obtained for the five material grades. This means that the five grades have similar strain-rate sensitivity.

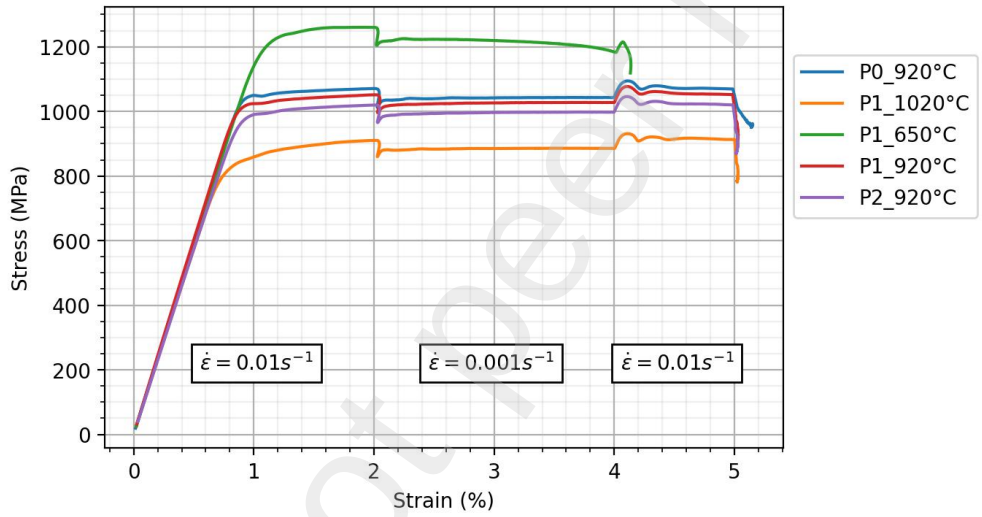

Figure 8: Stress-train curves of tensile tests. Strain rate was $10^{-2}\,\text{s}^{-1}$ for strain 0-2 % and 4-5 % and strain rate was $10^{-3}\,\text{s}^{-1}$ for strain 3-4 %. Strain was maintain at 5 % for 5 minutes for relaxation testing. Sample $P_1\_650°C$ broke outside the gauge of extensometer before relaxation step.

Table 2: Results of microstructural analysis and mechanical properties for the five studied grades.

Grade	$P_0\_920°C$	$P_1\_1020°C$	$P_1\_650°C$	$P_1\_920°C$	$P_2\_920°C$	Forged bimodal [28]
Grain size (µm)	1.6	200	0.4	1.6	1.6	15-20
Grain type	α-lamellae	$\alpha+\beta$ colony	α-lamellae	α-lamellae	α-lamellae	
Present phases	$\alpha+\beta$	$\alpha+\beta$	α', $\alpha+\beta$	$\alpha+\beta$	$\alpha+\beta$	α_p, $\alpha+\beta$
Porosity (%)	0.000	≈ 0.001	≈ 0.001	≈ 0.001	≈ 1	
Yield stress 0.2 % (MPa)	1047	850	1235	1024	992	930
Viscous stress (MPa)	113	132		138	150	
Microhardness (HV)	368 ± 9	321 ± 21	374 ± 6	352 ± 7	338 ± 4	

3.3. VHCF testing results

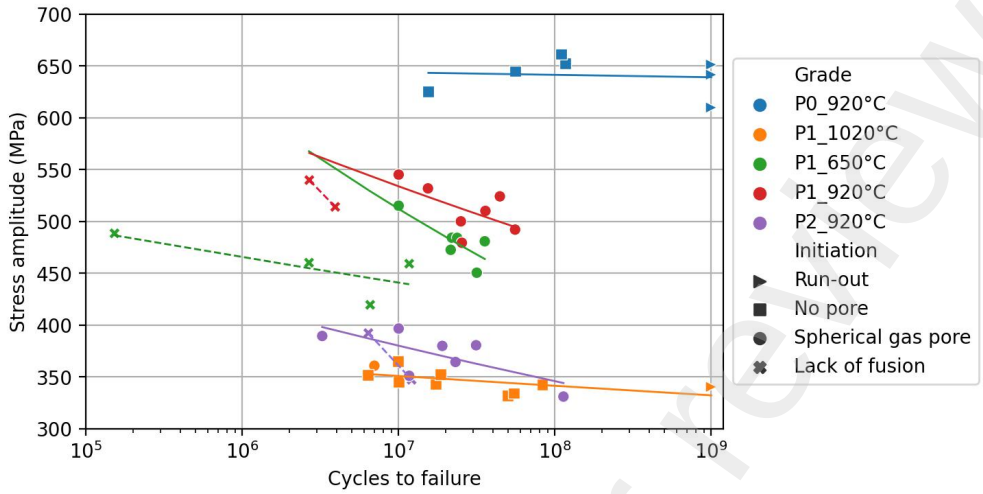

Figure 9: SN curves obtained using ultrasonic fatigue machine. Results are presented according to material grade and type of defect at fatigue crack initiation. Mean curves corresponds to best fitted power law for samples from the same grade. For P_1_650°C, P_1_920°C and P_2_920°C grades, two power laws were calculated according to the type of defect at fatigue crack initiation.

Figure 9 presents the stress amplitude to cycles to failure (SN) curves of the ultrasonic fatigue test results. These ones are presented according to the material grade of specimen and the type of fatigue crack initiation. Among grades with a P_1 porosity, P_1_920°C has the highest fatigue strength and P_1_1020°C the lowest. Microstructural changes between these two grades lead to a 180 MPa drop in VHCF resistance. The stress relieved P_1_650°C has a fatigue strength close but lower than P_1_920°C. As expected, fatigue strength decrease with porosity level for a constant grain size. Porosity in P_2_920°C specimens lead to a 260 MPa drop in fatigue strength at 10^7 cycles as compared to P_0_920°C. SN curves for P_1_920°C, P_1_650°C and P_2_920°C grades do not show any asymptotic behavior whereas the other does. These correspond to grades for which initiation was porosity-induced. In Figure 9, curves of fitted power law are represented for each grade. SN curves of grades P_1_920°C and P_1_650°C present two modes according to the type of pore at initiation. These curves are therefore associated with a large scatter.

Figure 10 shows the longitudinal stress amplitude field and the location of initiation sites on ultrasonic fatigue specimens. This stress amplitude field is scaled by the average stress amplitude over the mid-section. The majority of crack initiations were internal. Figure 10 shows that the higher the local stress amplitude, the more frequent is the location of fatigue crack initiation, although several other parameters such as the pores size, the pore shape or the local microstructure may influence this location. Similarly to the results of Heinz et al. [37], distance between surface and crack initiation $d_{surface}$ is lower than 640 µm for 70 % of specimens, which represent half of the section area. However, the amplitude of the longitudinal stress in this zone is only $\approx$ 5 % greater than the amplitude of the stress on the axis of the specimen. Longitudinally along the specimen, maximum distance between crack initiation site and mid-section of sample was 2.7 mm. Within this range, local stress determined using finite element analysis is

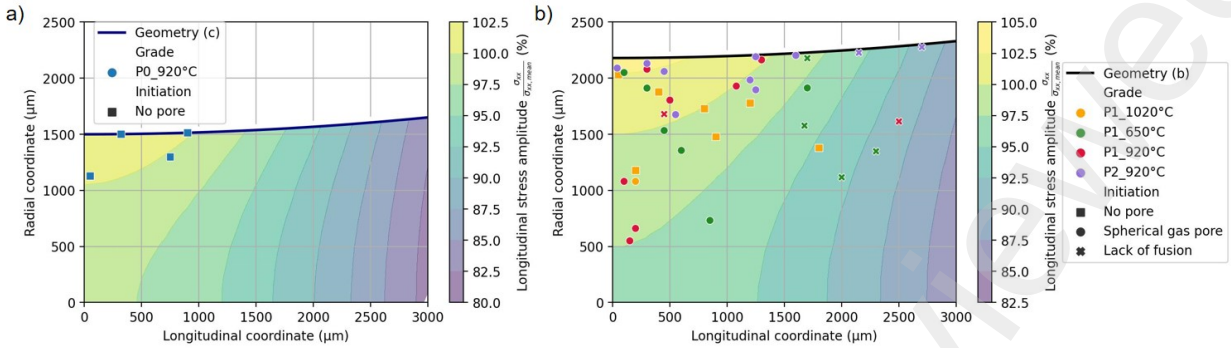

Figure 10: Longitudinal stress amplitude field and location of fatigue crack initiation sites: a) on ultrasonic fatigue specimens used for P_0_920°C specimens (geometry (c) in Figure 3); b) on ultrasonic fatigue specimens used for others specimens (geometry (b) in Figure 3). Stress amplitude field is scaled by the average stress amplitude over the mid-section. Longitudinal coordinate corresponds to the distance between crack initiation site and the mid section of fatigue sample. Radial coordinate corresponds to the distance between crack initiation site and main axis of fatigue specimen.

close ($discrepancy < 10$ %) to the one in longitudinally mid-section (Figure 10). Within all fatigue specimens, three types of fatigue crack initiations were observed: initiation around spherical gas pore (blowhole or keyhole), initiation around lack of fusion pore, initiation region without visible pore (Figure 11). One can see in Figure 10, that the type of initiation (ie. microstructure or porosity-induced) is not related to the local stress but to the tested grade. The most common case is initiation around spherical gas pore. Crack initiated always around pores and without microstructural facets in grades P_1_650°C, P_1_920°C and P_2_920°C. For these ones, size of critical pores are presented in Figure 12 using Gumbel's reduced variate. In P_1_650°C and P_1_920°C specimens, fatigue cracks initiated either on internal spherical blowhole pores which size range from 21 to 40 µm or on internal lack of fusion pores which size range from 76 to 200 µm (Figure 11.a-b). One can see in Figure 9 a drop of fatigue life for those grades when crack initiated on lack of fusion pores. The standard deviation associated with a log-normal distribution of stresses at 10^7 cycles is 20 MPa (resp. 16 MPa) for P_1_650°C (resp. P_1_920°C) grade. In P_2_920°C samples, fatigue cracks initiated on large keyhole pores (90 to 156 µm) or on lack of fusion pores (249 and 644 µm) (Figure 11.c-d). Although lack of fusion pores are much larger, types of critical pore seem not to affect fatigue life of P_2_920°C specimens (Figure 9). Due to the high density of pores in P_2_920°C samples, $d_{surface}$ is always lower than 500 µm and half of initiations can be considered as subsurface ones for which $\sqrt{Area_{eff}} > d_{surface}$ (Figure 10). The largest critical defect ($\sqrt{Area_{eff}} = 644$ µm) was a group of several interacting lack of fusion pores as defined in $\sqrt{Area_{eff}}$ method (Figure 11.c). On fracture surfaces of P_1_1020°C samples, microstructural facets are always visible and no pore are visible in 9 out of 10 specimens. Largest facets are as large as grains (≈ 200 µm). $\alpha + \beta$ lamellae are visible on these facets. For one P_1_1020°C specimen, a 12 µm spherical pore within a facet is present on fracture surface (Figure 11.e). No pore nor facets are visible on fracture surface of P_0_920°C specimens (Figure 11.f). This means that pores were effectively eliminated during HIP process. Furthermore, the two P_0_920°C specimens that had the lowest fatigue life were associated with a surface crack initiation whereas it was internal for the others. In this study, for all specimens,

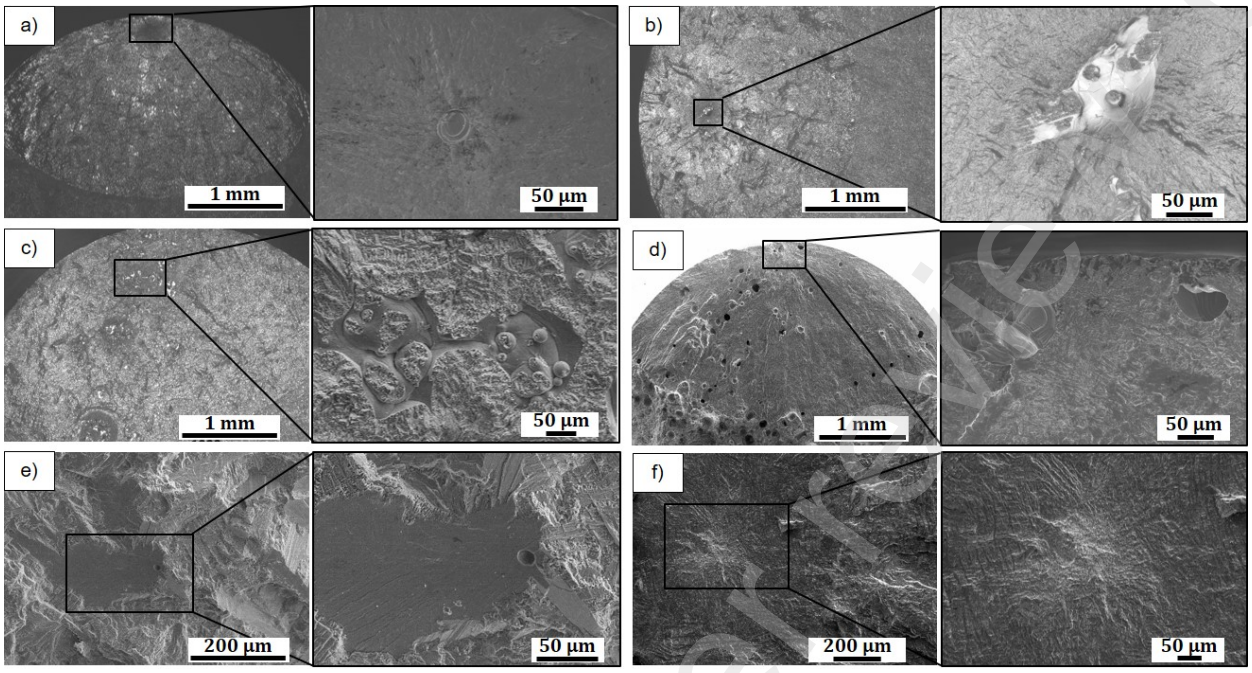

Figure 11: Optical and scanning electronic micrographs of fracture surfaces with different types of crack initiation. a) Initiation on a spherical gas pore in a P_1_650°C specimen. b) Initiation on a lack of fusion pore in a P_1_650°C specimen. c) Initiation on a group of interacting lack of fusion pores in a P_2_920°C specimen. d) Initiation on a keyhole pore in a P_2_920°C specimen. e) Initiation with large microstructural facets in P_1_1020°C specimen. f) Initiation without pore nor large microstructural facets in P_0_920°C specimen.

a dark area, also named fine granular area, was observed using optical microscopy near fatigue crack initiation zone. Its size was 150-300 µm for all specimens except for P_1_1020°C specimens in which it was close to 1000 µm.

4. Discussion

4.1. Process variability and effect of porosity

Although the same machine and powder batch were used, significant process variability can be found between printing batches. As mentioned earlier, two types of critical defect were observed: spherical gas pores and lack of fusion pores. Specimens that initiated from lack of fusion pores came from two out of the five printing batchs. One P_1_650°C from a flawed batch was scanned using microtomography and several large and flat pores (i.e. lack of fusion pores) were detected. These pores were located at close vertical coordinates meaning that a problem appeared during LPBF process at this layer. No special event was detected in the manufacturing data apart from an early filter clogging. In this study, lack of fusion pores visible on fractographic images are relatively flat. Their size along printing direction is small compared to the ones along the two horizontal directions. However, as they are not elongated in one horizontal direction, they do not correspond to unmelted area in between laser tracks (Figure 11 and Figure 12). They seems to be related either to local lack of powder possibly due to droplet fallen on powder bed or to instantaneous insufficient laser energy. As explained in [11], droplets and nanocondensates present in the vapor plume can reduce the laser

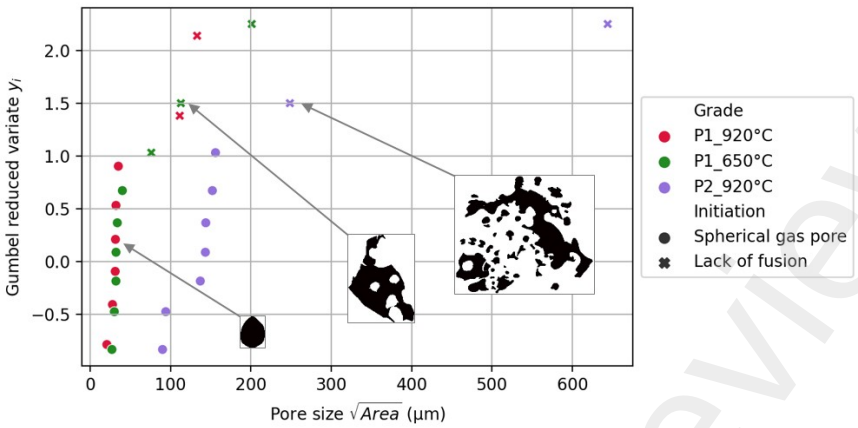

Figure 12: Gumbel distribution of the size of critical pores. Results are presented according to material grade and type of pore at fatigue crack initiation. Some representative shape of critical defect are represented.

energy brought to the powder and cause lack of fusion pores. However, P_0_920°C samples from flawed batches were associated with a microstructure-induced fracture. Two P_0_920°C samples from flawed batches were also scanned. No pore was detected within the data meaning that pores were effectively sealed by HIP process. Overall, VHCF fatigue testing results clearly discriminated samples containing lack of fusion pores although process data could not predict their formation. A possible practice when printing structural parts using LPBF, would be to print one or two ultrasonic fatigue test pieces within the same batch in order to validate the batch integrity.

In Figure 12, distribution of critical pore is not linear in Gumbel's space whereas the distribution obtained using microtomography and block maxima method is linear (Figure 7). The first one is not linear because two types of pores with very different size are considered. The second distribution is linear even when lack of fusion pores were present in the part. Indeed, as lack of fusion pores are relatively flat, their effective size $\sqrt{Area_{eff}}$ is much larger than $\sqrt[3]{Volume}$.

The effect of pores on the fatigue strength can be analyzed using Kitagawa-Takahashi (KT) diagram [4]. In this diagram, the plotted models should discriminate the finite and infinite fatigue life domains. Figure 13 shows the KT diagram with data for specimens from the grades with a microstructure obtained at 920°C. Data from P_1_650°C grade were also plotted as the microstructure and microhardness of this grade is close to the ones of 920°C grades. In this diagram, the size of critical defect is defined as $\sqrt{Area_{eff}}$ when initiation was porosity-induced. For visualization purpose, size of defect was set to 1 µm for P_0_920°C specimens. In Figure 13, the stress amplitude is the equivalent stress amplitude at 10^7 cycle. It is obtained using fitted power law calculated for samples with the same grade and the same type of pore at initiation. For each sample the equivalent stress is the stress where the respective mean curve, shifted so that it passes through the considered point, cross 10^7 cycle. The distinction according to both the grade and the type of pore at initiation allows take into account the bi-modal aspect of the SN curves of these grades (Figure 9). Three models are represented in Figure 13: the original KT's model, El-Haddad's model [38] and Murakami's

model [5]. The original KT diagram considers two fracture modes. For high stresses and low defect size, fatigue limit corresponds to the one of the defect-free material $\sigma_{a,lim}$. For lower stresses and defect size larger than the critical size, fatigue limit ensues from fatigue crack propagation threshold. El-Haddad's and Murakami's models are based on KT's one and differ for defect size close to the critical defect size for which short-crack effects cause failure in the safe domain of KT's model. El-Haddad's model accounts for this by adding a fictive length to the real defect size. Murakami's model corresponds to a short crack propagation threshold based on the hardness of the material. In this study, fatigue limit of the defect-free material was set to $\sigma_{a,lim} = 620\,\text{MPa}$ which corresponds to the fatigue limit of $P_0\_920°C$ grade. The three models take into account the threshold stress intensity factor for long crack propagation ΔK_{th}. Experimental values of ΔK_{th} ranging from 3.48 to 4.6 $\text{MPa}\,\text{m}^{0.5}$ were determined for a load ratio $R = 0.1$ [12][39][40]. Using Walker's equation, Leuders et al. [40] calculated values of ΔK_{th} ranging from 7.8 to 8.5 $\text{MPa}\,\text{m}^{0.5}$ for $R = -1$. Furthermore, the internal nature of defect considered in this study can influence the selected threshold value. ΔK_{th} was here set to 7 $\text{MPa}\,\text{m}^{0.5}$ leading to a critical defect size of 41 µm. In this study, size of spherical gas pore was often close to the critical defect size for which short crack effects become predominant. Recently, the fatigue crack growth model proposed in [30] highlighted the impact of crack closure effects when defect size is close to critical defect size for LPBF-Ti-6Al-4V. Therefore, El-Haddad and Murakami models better represent our data. One can notice that the types of pore at initiation clearly discriminate our data even though an equivalent stress at a constant fatigue life is used. This means that the shape of defect affect the fatigue limit. Indeed, the irregular shape of lack of fusion pores cause locally higher stress concentrations that can lead to a lower fatigue strength. Furthermore, $P_1\_650°C$ and $P_1\_920°C$ data are not discriminated in Figure 13. This means that the applied stress and the size of defect have a greater influence on fatigue strength compared to the microstructural differences between these grades. In relation to the microstructure-induced fatigue crack initiation of $P_1\_1020°C$ grade, fatigue strength of this grade corresponds to the defect-free fatigue resistance for this microstructure which is 290 MPa lower than the one of the $920°C$ microstructure.

4.2. Effect of the microstructure

Figure 14 shows the effect of thermal treatment on microhardness, fatigue strength and grain size. Fatigue strength and hardness values are the ones of P_1 grades. Error bars on microhardness curve correspond to the standard deviation over the 10 microhardness measurements performed on each grade. Mean fatigue strength is the stress at 10^7 cycles of the fitted power law for samples of the grade that do not initiate on lack of fusion pore (Figure 9). Error bars on fatigue strength curve correspond to the standard deviation associated with a lognormal dispersion around fitted power laws. Fatigue strength does not vary monotonically with hardness or yield stress as generally observed [5]. According to hardness measurement, $P_1\_650°C$ grade should have an higher fatigue strength than $P_1\_920°C$. This can not be explained by the size of critical defect as mean size of critical spherical gas pore was 32 µm for both grades. The relatively low fatigue resistance of $P_1\_650°C$ grade could be related to martensitic α' present in this grade and not in $P_1\_920°C$ grade [35]. Indeed, α' phase is more brittle than α phase and $P_1\_650°C$ specimen used for tensile test did

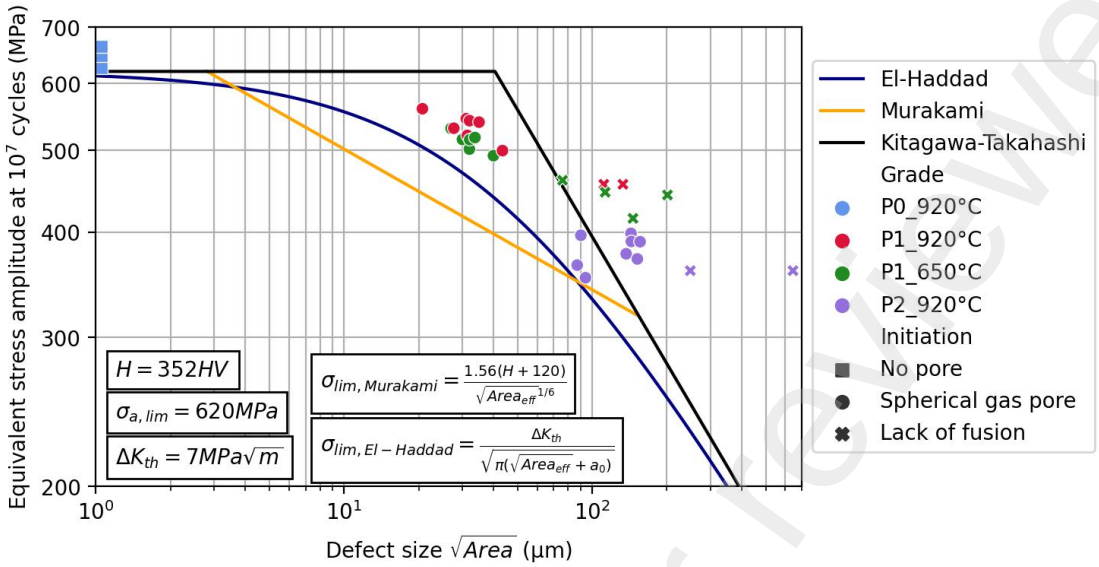

Figure 13: Kitagawa-Takahashi diagram representing the critical defect size $\sqrt{Area_{eff}}$ and the equivalent stress amplitude at 10^7 cycles. El-Haddad's, Murakami's and Kitagawa-Takahashi's models are represented. Murakami's and Kitagawa-Takahashi's models are calculated with the factor corresponding to internal crack initiation.

not reach 5 % of uniform strain. Moreover, residuals stresses can cause this results as they are not fully relaxed in P_1_650°C specimens [13] whereas they are in P_1_920°C ones [12].

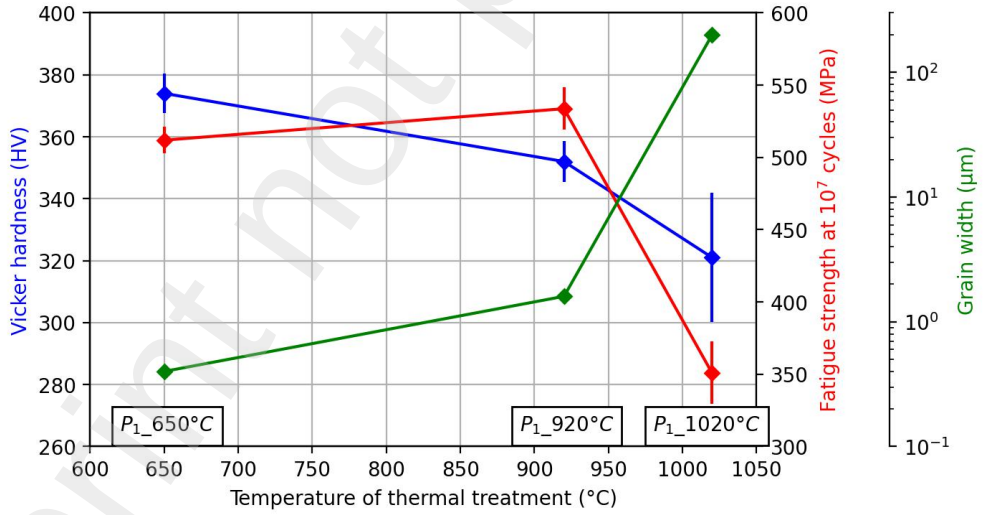

Figure 14: Effect of temperature of thermal treatment on the microhardness, the grain size and the fatigue strength. Fatigue strength values are the ones of grades with the same porosity level P_1 and without considering specimens that initiated on lack of fusion pores.

Cracks initiated on pores for P_1_650°C, P_1_920°C and P_2_920°C grades that have relatively fine microstructures. For P_0_920°C, for which initiation was microstructure-induced, width of lamellae is 1.6 µm and no pore larger than several µm was detected in microtomographic data. Specimen of group P_1_1020°C contains pores but have large

grains leading to a microstructure-induced initiation. This is also true for P_1_1020°C specimens printed in the flawed batches, although large lack of fusion pores might be present within this. Overall, for all studied grades crack initiated on microstructural aspect and without visible pore when grain size was larger than pore size. Furthermore, in P_1_1020°C grade, width of lamellae was smaller than pores whereas grain width was larger. Microstructural facets as large as grains are visible on P_1_1020°C fracture surface. Therefore, lamellar colonies (i.e grains) are the main microstructural barrier to fatigue crack. This is in accordance with the results from Nalla et al. [41] in which crack path was deflected around lamellar colonies of a forged Ti-6Al-4V.

5. Conclusions

The major goal of this study was to analyze the sensitivity of VHCF properties in accelerated 20 kHz fatigue testing to both porosity and microstructure variations in AM material. The main findings of this work were:

- Extremely low porosity was achieved on LPBF-Ti-6Al-4V. Process variability was significant in between printing batches but limited within batches. Few specimens can be tested using ultrasonic fatigue machine to monitor batch quality.
- LPBF specimens with a reproducible target porosity were obtained by adjusting the laser scan strategy. LPBF specimens with a target microstructure without any changes in porosity were obtained by adjusting subsequent heat treatments.
- Chosen HIP treatment (2h, 2000 bar at 920°C) effectively sealed both spherical gaz pores and lack of fusion pores, which led to superior fatigue properties.
- Fast fatigue testing using ultrasonic fatigue was sensitive to both porosity and microstructure variations. It was therefore suited for AM parameter optimization. Furthermore, monotonic testing were not suited for parameter optimization. Indeed, porosity had a limited impact on monotonic yield stress as compared to the porosity-induced drop in VHCF resistance.
- Size of pores and size of grains had a first order effect on VHCF resistance of LPBF-Ti-6Al-4V. Indeed, fatigue crack initiation was porosity-induced when largest pores were larger that grains and microstructure-induced when grains were larger than largest pores. Moreover, SN curves of LPBF-Ti-6Al-4V grades for which fatigue crack initiation was microstructure-induced presented an asymptotic behavior in the VHCF regime whereas the ones for which fatigue crack initiation was porosity-induced did not present it.
- The optimal temperature of post-treatment for VHCF properties of LPBF-Ti-6Al-4V was shown to be close to 920°C.

Acknowledgment

This work was supported by ONERA and CETIM through their contribution in Additive Factory Hub (AFH), a French research consortium working on metallic additive manufacturing. The authors acknowledge C. Rouaud and C. Lopes who performed thermal treatments of test pieces, Y. Gruchy for the machining of test pieces, N. Horezan and A. Bachelier-Locq for SEM/EBSD analysis and M. Bornert for micro-tomography data analysis.

Declaration of Competing Interest

The authors declare that they have no known competing financial interests or personal relationships that could have appeared to influence the work reported in this paper.

References

[1] G. Kasperovich, J. Hausmann, Improvement of fatigue resistance and ductility of TiAl6v4 processed by selective laser melting 220 202–214. doi:10.1016/j.jmatprotec.2015.01.025.
URL https://linkinghub.elsevier.com/retrieve/pii/S0924013615000278

[2] P. Kumar, O. Prakash, U. Ramamurty, Micro-and meso-structures and their influence on mechanical properties of selectively laser melted ti-6al-4v 154 246–260. doi:10.1016/j.actamat.2018.05.044.
URL https://www.sciencedirect.com/science/article/pii/S1359645418304117

[3] V.-D. Le, E. Pessard, F. Morel, F. Edy, Interpretation of the fatigue anisotropy of additively manufactured TA6v alloys via a fracture mechanics approach 214 410–426. doi:10.1016/j.engfracmech.2019.03.048.
URL https://linkinghub.elsevier.com/retrieve/pii/S0013794418311664

[4] H. Kitagawa, S. Takahashi, Applicability of fracture mechanics to very small cracks or the cracks in the early stage. 2nd 627–631.

[5] Y. Murakami, Metal Fatigue: Effects of Small Defects and Nonmetallic Inclusions., Elsevier Science Publishing Co Inc, OCLC: 1096516382.

[6] T. Spears, S. Gold, In-process sensing in selective laser melting (SLM) additive manufacturing 5. doi:10.1186/s40192-016-0045-4.

[7] H. Shipley, D. McDonnell, M. Culleton, R. Coull, R. Lupoi, G. O'Donnell, D. Trimble, Optimisation of process parameters to address fundamental challenges during selective laser melting of ti-6al-4v: A review 128 1–20. doi:10.1016/j.ijmachtools.2018.01.003.
URL https://linkinghub.elsevier.com/retrieve/pii/S0890695518300233

[8] M. Tarik Hasib, H. E. Ostergaard, X. Li, J. J. Kruzic, Fatigue crack growth behavior of laser powder bed fusion additive manufactured ti-6al-4v: Roles of post heat treatment and build orientation 142 105955. doi:10.1016/j.ijfatigue.2020.105955.
URL https://linkinghub.elsevier.com/retrieve/pii/S0142112320304874

[9] B. Vrancken, L. Thijs, J.-P. Kruth, J. Van Humbeeck, Heat treatment of ti6al4v produced by selective laser melting: Microstructure and mechanical properties 541 177–185. doi:10.1016/j.jallcom.2012.07.022.
URL https://linkinghub.elsevier.com/retrieve/pii/S0925838812011826

[10] J. Yang, H. Yu, J. Yin, M. Gao, Z. Wang, X. Zeng, Formation and control of martensite in ti-6al-4v alloy produced by selective laser melting 108 308–318. doi:10.1016/j.matdes.2016.06.117.
URL https://linkinghub.elsevier.com/retrieve/pii/S0264127516308796

[11] T. de Terris, O. Andreau, P. Peyre, F. Adamski, I. Koutiri, C. Gorny, C. Dupuy, Optimization and comparison of porosity rate measurement methods of selective laser melted metallic parts 28 802–813. doi:10.1016/j.addma.2019.05.035.
URL https://linkinghub.elsevier.com/retrieve/pii/S2214860418307723

[12] S. Leuders, M. Thöne, A. Riemer, T. Niendorf, T. Tröster, H. Richard, H. Maier, On the mechanical behaviour of titanium alloy TiAl6v4 manufactured by selective laser melting: Fatigue resistance and crack growth performance 48 300–307. doi:10.1016/j.ijfatigue.2012.11.011.
URL https://linkinghub.elsevier.com/retrieve/pii/S014211231200343X

[13] A. K. Syed, B. Ahmad, H. Guo, T. Machry, D. Eatock, J. Meyer, M. E. Fitzpatrick, X. Zhang, An experimental study of residual stress and direction-dependence of fatigue crack growth behaviour in as-built and stress-relieved selective-laser-melted ti6al4v 755 246–257. doi:10.1016/j.msea.2019.04.023.
URL https://linkinghub.elsevier.com/retrieve/pii/S0921509319304691

[14] F. R. Kaschel, R. K. Vijayaraghavan, P. J. McNally, D. P. Dowling, M. Celikin, In-situ XRD study on the effects of stress relaxation and phase transformation heat treatments on mechanical and microstructural behaviour of additively manufactured ti-6al-4v 819 141534. doi:10.1016/j.msea.2021.141534.
URL https://www.sciencedirect.com/science/article/pii/S0921509321008030

[15] S. A. Etesami, B. Fotovvati, E. Asadi, Heat treatment of ti-6al-4v alloy manufactured by laser-based powder-bed fusion: Process, microstructures, and mechanical properties correlations 895 162618. doi:10.1016/j.jallcom.2021.162618.
URL https://www.sciencedirect.com/science/article/pii/S0925838821040287

[16] T. Vilaro, C. Colin, J. D. Bartout, As-fabricated and heat-treated microstructures of the ti-6al-4v alloy processed by selective laser melting 42 (10) 3190–3199. doi:10.1007/s11661-011-0731-y.
URL http://link.springer.com/10.1007/s11661-011-0731-y

[17] G. M. Ter Haar, T. Becker, D. C. Blaine, Influence of heat treatments on the microstructure and tensile behavior of selective laser melting-produced ti-6al-4v parts. 27 (3). doi:10.7166/27-3-1663.
URL http://sajie.journals.ac.za/pub/article/view/1663

[18] S. Cecchel, D. Ferrario, G. Cornacchia, M. Gelfi, Development of heat treatments for selective laser melting ti6al4v alloy: Effect on microstructure, mechanical properties, and corrosion resistance 22 (8). doi:10.1002/adem.202000359.

[19] C. Bathias, P. C. Paris, Gigacycle fatigue in mechanical practice, Marcel Dekker.

[20] P. Li, D. Warner, A. Fatemi, N. Phan, Critical assessment of the fatigue performance of additively manufactured ti–6al–4v and perspective for future research 85 130–143. doi:10.1016/j.ijfatigue.2015.12.003.
URL https://linkinghub.elsevier.com/retrieve/pii/S0142112315004399

[21] S. Leuders, T. Lieneke, S. Lammers, T. Tröster, T. Niendorf, On the fatigue properties of metals manufactured by selective laser melting – the role of ductility 29 (17) 1911–1919. doi:10.1557/jmr.2014.157.
URL http://link.springer.com/10.1557/jmr.2014.157

[22] P. R. da Costa, M. Sardinha, L. Reis, M. Freitas, M. Fonte, Ultrasonic fatigue testing in as-built and polished ti6al4v alloy manufactured by SLM 100024doi:10.1016/j.finmec.2021.100024.
URL https://www.sciencedirect.com/science/article/pii/S2666359721000159

[23] J. Günther, D. Krewerth, T. Lippmann, S. Leuders, T. Tröster, A. Weidner, H. Biermann, T. Niendorf, Fatigue life of additively manufactured ti–6al–4v in the very high cycle fatigue regime 94 236–245. doi:10.1016/j.ijfatigue.2016.05.018.
URL https://linkinghub.elsevier.com/retrieve/pii/S0142112316301207

[24] L. Du, X. Pan, G. Qian, L. Zheng, Y. Hong, Crack initiation mechanisms under two stress ratios up to very-high-cycle fatigue regime for a selective laser melted ti-6al-4v 149 106294. doi:10.1016/j.ijfatigue.2021.106294.
URL https://www.sciencedirect.com/science/article/pii/S0142112321001547

[25] A. Tridello, J. Fiocchi, C. Biffi, G. Chiandussi, M. Rossetto, A. Tuissi, D. Paolino, VHCF response of heat-treated SLM ti6al4v gaussian specimens with large loaded volume 18 314–321. doi:10.1016/j.prostr.2019.08.171.
URL https://linkinghub.elsevier.com/retrieve/pii/S2452321619303816

[26] E. Wycisk, S. Siddique, D. Herzog, F. Walther, C. Emmelmann, Fatigue performance of laser additive manufactured ti–6al–4v in very high cycle fatigue regime up to 109 cycles 2. doi:10.3389/fmats.2015.00072.

URL http://journal.frontiersin.org/Article/10.3389/fmats.2015.00072/abstract

[27] G. Qian, Y. Li, D. S. Paolino, A. Tridello, F. Berto, Y. Hong, Very-high-cycle fatigue behavior of ti-6al-4v manufactured by selective laser melting: Effect of build orientation 136 105628. doi:10.1016/j.ijfatigue.2020.105628.

[28] R. Morrissey, T. Nicholas, Staircase testing of a titanium alloy in the gigacycle regime 28 (11) 1577–1582. doi:10.1016/j.ijfatigue.2005.10.007.
URL http://www.sciencedirect.com/science/article/pii/S0142112306000922

[29] Y. Hu, S. Wu, Z. Wu, X. Zhong, S. Ahmed, S. Karabal, X. Xiao, H. Zhang, P. Withers, A new approach to correlate the defect population with the fatigue life of selective laser melted ti-6al-4v alloy 136 105584. doi:10.1016/j.ijfatigue.2020.105584.
URL https://linkinghub.elsevier.com/retrieve/pii/S0142112320301158

[30] N. Macallister, T. H. Becker, Fatigue life estimation of additively manufactured ti-6al-4v: Sensitivity, scatter and defect description in damage-tolerant models 237 118189. doi:10.1016/j.actamat.2022.118189.
URL https://www.sciencedirect.com/science/article/pii/S1359645422005705

[31] W. Chi, G. Li, W. Wang, C. Sun, Interior initiation and early growth of very high cycle fatigue crack in an additively manufactured ti-alloy 160 106862. doi:10.1016/j.ijfatigue.2022.106862.
URL https://www.sciencedirect.com/science/article/pii/S0142112322001372

[32] H. Mughrabi, On 'multi-stage' fatigue life diagrams and the relevant life-controlling mechanisms in ultrahigh-cycle fatigue 25 (8) 755–764. doi:10.1046/j.1460-2695.2002.00550.x.
URL https://onlinelibrary.wiley.com/doi/abs/10.1046/j.1460-2695.2002.00550.x

[33] V. Jacquemain, N. Ranc, C. Cheuleu, V. Michel, V. Favier, O. Castelnau, D. Vinci, D. Thiaudiere, C. Mocuta, Estimation of stress in specimens loaded with ultrasonic fatigue machines 153 106474. doi:10.1016/j.ijfatigue.2021.106474.
URL https://www.sciencedirect.com/science/article/pii/S0142112321003327

[34] H. Masuo, Y. Tanaka, S. Morokoshi, H. Yagura, T. Uchida, Y. Yamamoto, Y. Murakami, Influence of defects, surface roughness and HIP on the fatigue strength of ti-6al-4v manufactured by additive manufacturing 117 163–179. doi:10.1016/j.ijfatigue.2018.07.020.
URL https://linkinghub.elsevier.com/retrieve/pii/S0142112318303050

[35] F. R. Kaschel, R. K. Vijayaraghavan, A. Shmeliov, E. K. McCarthy, M. Canavan, P. J. McNally, D. P. Dowling, V. Nicolosi, M. Celikin, Mechanism of stress relaxation and phase transformation in additively manufactured ti-6al-4v via in situ high temperature XRD and TEM analyses 188 720–732. doi:10.1016/j.actamat.2020.02.056.
URL https://www.sciencedirect.com/science/article/pii/S1359645420301695

[36] F. X. Gil Mur, D. Rodríguez, J. A. Planell, Influence of tempering temperature and time on the alpha'-ti-6al-4v martensite 234 (2) 287–289. doi:10.1016/0925-8388(95)02057-8.
URL https://www.sciencedirect.com/science/article/pii/0925838895020578

[37] S. Heinz, F. Balle, G. Wagner, D. Eifler, Analysis of fatigue properties and failure mechanisms of ti6al4v in the very high cycle fatigue regime using ultrasonic technology and 3d laser scanning vibrometry 53 (8) 1433–1440. doi:10.1016/j.ultras.2013.03.002.
URL http://www.sciencedirect.com/science/article/pii/S0041624X13000644

[38] M. H. El Haddad, T. H. Topper, K. N. Smith, Prediction of non propagating cracks 11 (3) 573–584. doi:10.1016/0013-7944(79)90081-X.
URL https://www.sciencedirect.com/science/article/pii/001379447990081X

[39] E. Wycisk, A. Solbach, S. Siddique, D. Herzog, F. Walther, C. Emmelmann, Effects of defects in laser additive manufactured ti-6al-4v on fatigue properties 56 371–378. doi:10.1016/j.phpro.2014.08.120.
URL http://www.sciencedirect.com/science/article/pii/S187538921400265X

[40] S. Leuders, M. Vollmer, F. Brenne, T. Tröster, T. Niendorf, Fatigue strength prediction for titanium alloy TiAl6v4 manufactured by selective laser melting 46 (9) 3816–3823. doi:10.1007/s11661-015-2864-x.
URL http://link.springer.com/10.1007/s11661-015-2864-x

[41] R. K. Nalla, R. O. Ritchie, B. L. Boyce, J. P. Campbell, J. O. Peters, Influence of microstructure on high-cycle fatigue of ti-6al-4v: Bimodal

vs. lamellar structures 33 (3) 899–918. doi:10.1007/s11661-002-0160-z.
URL https://doi.org/10.1007/s11661-002-0160-z